Geochemistry, Geophysics, Geosystems

RESEARCH ARTICLE
10.1029/2019GC008212

Key Points:
- Factor analyses are used to decipher sediment color reflectance data from the Southern Ocean for the first time
- Four factors control sediment color changes, indicative of useful core parameters and paleoenvironmental proxies
- Information on abyssal ocean ventilation, relative abundance of hematite and goethite, and water content were obtained from the color data

Supporting Information:
- Supporting Information S1
- Table S1
- Table S2
- Table S3
- Figure S1
- Figure S2
- Figure S3
- Data Set S1
- Data Set S2
- Data Set S3
- Data Set S4

Correspondence to:
L. Wu and R. Wang,
wuli@tongji.edu.cn;
rjwang@tongji.edu.cn

Citation:
Wu, L., Wang, R., Krijgsman, W., Chen, Z., Xiao, W., Ge, S., & Wu, J. (2019). Deciphering color reflectance data of a 520-kyr sediment core from the Southern Ocean: Method application and paleoenvironmental implications. *Geochemistry, Geophysics, Geosystems*, *20*, 2808–2826. https://doi.org/10.1029/2019GC008212

Received 17 JAN 2019
Accepted 24 APR 2019
Accepted article online 17 MAY 2019
Published online 20 JUN 2019

Deciphering Color Reflectance Data of a 520-kyr Sediment Core From the Southern Ocean: Method Application and Paleoenvironmental Implications

Li Wu[1], Rujian Wang[1], Wout Krijgsman[2], Zhihua Chen[3], Wenshen Xiao[1], Shulan Ge[3], and Jiawang Wu[1,2]

[1]State Key Laboratory of Marine Geology, Tongji University, Shanghai, China, [2]Department of Earth Sciences, Utrecht University, Utrecht, The Netherlands, [3]First Institute of Oceanography, State Oceanic Administration, Qingdao, China

Abstract Sediment color reflectance contains important information on paleoenvironmental changes. Such data are routinely measured on sediment cores from the Southern Ocean. Their usefulness, however, is undervalued. Here for the first time, color reflectance of an ~520-kyr sediment core retrieved off Prydz Bay (East Antarctica) was intensively investigated to correlate sediment color changes to changes in sediment compositions. Total carbon, total organic carbon, X-ray fluorescence-derived Fe/Ti and Br/Ti ratios, water content and mineral composition of sediment from this core, and color reflectance of another two sediment cores retrieved nearby were analyzed in this study. The raw reflectance data were transformed into their first-order derivatives and subjected to factor analysis algorithms. A four-factor model was selected to unmix the data set, explaining >80% of the total data variance. Its robustness is supported by similar factor analysis results from the other two cores. The four factors represent (from Factors 1–4) pulses of sedimentary Mn enrichment and Fe^{3+}/Fe^{2+} changes in clay minerals, relative content changes of colorless components, hematite and goethite, and water, respectively. Scores of Factor 1 show high spikes at glacial terminations, recording enhanced deglacial ventilation in the abyssal Southern Ocean. Scores of Factor 2 mainly reflect biogenic components and chlorite but are further complicated by refractory terrigenous organic carbon and Mn-oxides/-hydroxides. Higher Scores of Factor 3 occur mainly at peak interglacial intervals, associated with enhanced transport of sediment of Antarctic origin by oceanic currents. Water content (Factor 4) in the core sediment was significantly influenced by opal content and sediment grain size compositions.

1. Introduction

Color is the most conspicuous characteristic of sediment and has diagnostic values of sediment composition, texture, and structure (Balsam & Deaton, 1996; Debret et al., 2011; Weber et al., 2010). Using diffuse reflectance spectrophotometry (DRS) method on visible light band (i.e., 400–700 nm), color data can be cheaply, rapidly, quantitatively, and nondestructively obtained from sediment (Mix et al., 1992). The DRS technique produces a set of reflectance data on the visible light band and automatically transfers them into coordinates of color in CIE *La*b** chromaticity space (Nagao & Nakashima, 1992). The CIE *La*b** chromaticity space is a three-dimensional color space that approximates a cylinder (Billmeyer & Saltzman, 1981). Its vertical axis *L* refers to lightness, while *a** (i.e., from green to red) and *b** (i.e., from blue to yellow) are the Cartesian coordinates that define a quasi-circular hue-chroma space (i.e., a normal section of the cylinder) at any given *L* (Debret et al., 2011).

The *L*, *a**, and *b** values obtained from sediment color reflectance are useful as alternative indicators of various physical and geochemical parameters in paleoenvironmental studies, especially in the case of high-resolution analyses (Giosan et al., 2002; Heslop et al., 2007; Ji et al., 2005; Rein & Sirocko, 2002). Specifically, *L* value often highly correlates with biogenic carbonate content of sediments in low-latitude oceans (e.g., Balsam et al., 1999). Sometimes, *b** value can be used to reflect the distribution pattern of diatom export production in high-latitude oceans (e.g., Debret et al., 2006; Weber et al., 2012), while *a** value has been considered as a proxy for relative changes in concentrations of iron oxide/oxy-hydroxide minerals, and by inference, weathering intensity of loess deposits (e.g., Ji et al., 2005; Yang & Ding, 2003). In particular, some sedimentary components at very low concentrations that cannot be readily determined can be estimated via color reflectance data. For instance, hematite and goethite have been identified using the DRS

technique, even at concentrations as low as 0.01% by weight (Balsam et al., 2014; Cong et al., 2018; Deaton & Balsam, 1991; Ji et al., 2002; Lu et al., 2017).

Downcore analysis of the raw reflectance spectral data with appropriate mathematical methods can provide even more valuable information with respect to paleoenvironmental reconstructions (e.g., Balsam & Wolhart, 1993; Giosan et al., 2002; Heslop et al., 2007; Lu et al., 2017; Pan et al., 2014). The algorithms designed to deconvolve raw reflectance spectrum data include factor analysis (Balsam et al., 1995; Balsam & Wolhart, 1993), multiple regression (Balsam & Deaton, 1996; Pan & Chen, 2013), cluster analysis (Balsam et al., 2007), and nonnegative matrix factorization (Heslop et al., 2007). During recent decades, these methods have been widely applied in different environmental settings, such as the North Atlantic (Giosan et al., 2002), the tropical Atlantic (Balsam et al., 1995), the Mediterranean Sea (Heslop et al., 2007), the Argentine Basin (Balsam & Wolhart, 1993), the Amazon Fan (Balsam et al., 1997), the Blake Ridge (Balsam & Damuth, 2000), the Gulf of Mexico (Balsam & Beeson, 2003), the East Pacific Rise (Balsam & Deaton, 1996), the South China Sea (Pan et al., 2014; Pan & Chen, 2013), and the Lake El'gygytgyn, East Russia (Wei et al., 2014). In these studies, information on sedimentary composition, including carbonate, hematite/goethite, specific species of clay minerals (e.g., kaolinite and chlorite), organic matter, and even specific species of foraminifera were obtained by unmixing color reflectance data to infer paleoevironmental/paleoclimatic evolution (Balsam et al., 1997; Balsam & Damuth, 2000; Balsam & Deaton, 1996; Balsam & Wolhart, 1993; Giosan et al., 2002; Heslop et al., 2007; Pan et al., 2014; Wei et al., 2014). In the Southern Ocean, however, except for a few studies mentioned color reflectance as auxiliary data (e.g., Grützner et al., 2003; Weber et al., 2012), almost no work focusing on sediment color exists so far. The Southern Ocean is a key area in global marine carbon cycling (Anderson et al., 2009; Jaccard et al., 2013, 2016) but has relatively few paleoenvironmental records. Studies of sediment color reflectance will enrich paleoenvironmental proxies that can be used in this key region.

In this study, we present color reflectance data from a well-dated sediment core ANT30/P1-02 retrieved from Prydz Bay, East Antarctica. Based on a novel factor analysis, we investigate the associations between sediment color and sediment compositions in the study area and to further link changes in sediment color to changes in local and regional paleoenvironment. To achieve this goal, we also present a suite of data from this core, including X-ray diffraction (XRD)-derived bulk sediment mineral composition, total carbon (TC, to estimate calcium carbonate content), total organic carbon (TOC), X-ray fluorescence (XRF)-scanning-derived Fe/Ti and Br/Ti (a proxy for organic carbon in marine sediment; Mayer et al., 2007; Ziegler et al., 2013) count ratios, and water content. Previous studies have suggested that these materials/components play important roles in affecting sediment colors (Balsam et al., 1998, 1999, 2014; Balsam & Deaton, 1991; Cong et al., 2018; Giosan et al., 2002; Lu et al., 2017; Lyle, 1983; Reynolds et al., 2014). For example, chlorite (Heslop et al., 2007), carbonate/opal (Balsam et al., 1999), organic matter (Balsam & Deaton, 1991), and water content (Balsam et al., 1998; Balsam & Deaton, 1991) affect lightness of sediment significantly, while Fe oxides/oxy-hydroxides determine the hue of sediment in most cases (Deaton & Balsam, 1991; Giosan et al., 2002; Ji et al., 2002; Lyle, 1983). Previous sedimentological and geochemical analyses on this core have generated a robust age model (Wu et al., 2017) and provided robust proxies for global climate change (Wu et al., 2017, 2018). In addition to the data set from core ANT30/P1-02, color reflectance data of two other sediment cores ANT30/P1-03 and ANT29/P4-01 were also included to support this study.

In summary, this work is designed as a case study to investigate the correlation between color and sediment composition and to understand the impact of paleoevironmental changes on the color of marine sediment from the Southern Ocean. To our knowledge, this is the first study focusing on color reflectance data from Late Quaternary sediment collected from high latitudes of the Southern Ocean.

2. Regional Environmental Setting

Prydz Bay is the third largest embayment around Antarctica with an area of ~80,000 km^2 (Figure 1). It is situated between 65°E and 80°E facing the southern Indian Ocean. The bay is at the seaward terminus of a major Mesozoic (or even older) graben structure—the Lambert Graben—which is currently occupied by the Lambert Glacier and the Amery Ice Shelf system (Passchier et al., 2003).

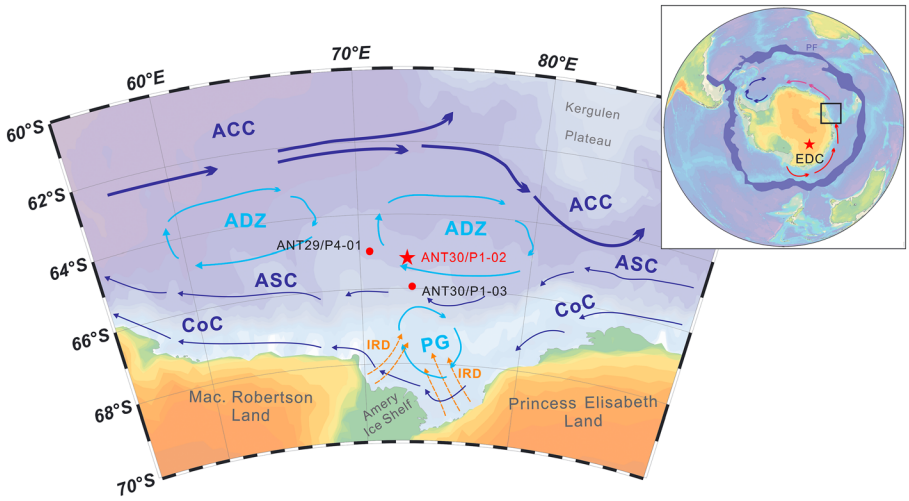

Figure 1. Map of the study area, showing the location of studied sediment cores ANT30/P1-02 (P1-2, as a red filled pentagram), ANT30/P1-03, and ANT29/P 4-01 (P1-2 and P4-1, as red filled circles). The tracks of IRD (i.e., ice-rafted debris) and oceanic currents are after Cooper and O'Brien (2004), Forsberg et al. (2008), and Meijers et al. (2010): CoC (Antarctic Coastal Current), PG: Prydz Gyre. ASC: Antarctic Slope Current. ADZ: Antarctic Divergence Zone. ACC: Antarctic Circumpolar Current. The zoom-out view on the upper right shows the Prydz Bay area (black box) in the Southern Ocean. Arrows with red, purple, and blue colors indicate major flow paths of AABW of Ross Sea and Adele Land, Prydz Bay, and Weddell Sea origins, respectively, according to Williams et al. (2008) and Meijers et al. (2010). The red-filled pentagram EDC shows the site of EPICA Dome C ice core (EPICA-Community-Members, 2004). The blue-shaded area denotes the modern Antarctic Polar Front zone (APF) modified after Röthlisberger et al. (2010).

Around Prydz Bay, the oceanic current system is composed of five branches (Bindoff et al., 2000; Cooper & O'Brien, 2004; Nunes Vaz & Lennon, 1996). The Antarctic Coastal Current (CoC) flows westward, bringing in cold waters from the east. The Antarctic Slope Current (ASC) driven by the Southern Easterly Wind (SEW) also flows from east to west but over the continental slope (Mathiot et al., 2011). Between the CoC and the ASC, the clockwise rotating Prydz Gyre (PG) mainly flows over the continental shelf. North of the ASC, the cyclonic Antarctic Divergence Zone (ADZ) represents a series of mesoscale eddies forming under the shear stress of the Southern Westerly Wind (SWW) and the SEW. It can intrude onto the shelf and brings up the relatively warm and salty Antarctic Deep Water (Yabuki et al., 2006). Farther offshore, the northern Antarctic Circumpolar Current (ACC) flows eastward and connects Southern Ocean with other oceans.

3. Materials and Methods

3.1. Sediment Cores and Age Model

Sediment cores ANT29/P4-01 (P4-1), ANT30/P1-02 (P1-2), and ANT30/P1-03 (P1-3) were retrieved off Prydz Bay during the 29th and 30th Chinese Antarctica Expedition on board R/V *Xuelong* in 2013 and 2014, respectively (Table 1). The color of the cores varies between grey and brown, showing distinct changes with depth. Sediments mainly consist of massive clayey silt or silty clay with minor sand (63–2,000 μm) and a few randomly distributed dropstones (>2 mm). No sign of significant bioturbation was observed throughout these cores.

Age models with orbital timescale resolution of these cores were established by Wu et al. (2017) through tuning their export production records to LR04-delta^{18}O stack, given that there are not enough foraminifera in the sediment. The age models are supported by Relative Paleo-Intensity data from the same sediment cores (Wu et al., 2017). These cores span the last ~500 kyr, with average sedimentation rates ranging from 0.9 to 1.19 cm/kyr (Table 1). Core P1-2 is our major focus of this study,

3.2. Methods

The analytical methods used in this study include color reflectance measurements and subsequent First-order Derivative Spectrum (FDS) and Factor Analyses, TC, TOC, and water content measurements, XRD bulk sediment mineral compositions, and Fe/Ti count ratio measurement. All the analyses and

Table 1
Information of Sediment Cores Used in This Study

Site	Longitude (°E)	Latitude (°S)	Water depth (m)	Core length (cm)	Age span (kyr)	Average LSR[a] (cm/kyr)
P1-3	73.02	65.99	2,542	599	510	1.17
P1-2	72.94	65.01	2,860	624	523	1.19
P4-1	70.69	64.92	3,162	421	495	0.85

[a]LSR: linear sedimentation rate.

measurements were conducted on core P1-2, while only color reflectance was measured on cores P1-3 and P4-1. All these analyses and measurements were carried out at the State Key Laboratory of Marine Geology, Tongji University.

3.2.1. Color Reflectance Analyses

Color reflectance was measured using a Minolta spectrophotometer CM-2002 at 1-cm increment as follows: The cores were tightly sealed and stored under −2 °C conditions (for less than a month) immediately after collection to prevent oxidation until color reflectance measurements were made. Cores were then split into two equal halves. The working half was covered by a transparent film, which was adjusted to tightly fit the smooth split core surface. Color reflectance was measured on the film-covered surface after each core reached room temperature.

Minolta spectrophotometer CM-2002 provides quantitative measurements of the visible light spectrum from 400 to 700 nm and automatically transfers it into the CIE La^*b^* color space (Nagao & Nakashima, 1992). All spectra were measured relative to a black background and a standard white plate made with barium sulfate under a standard illumination condition.

The Hue is defined by the angle between the coordinates b^* and a^* as follows (Giosan et al., 2002; Wei et al., 2014):

$$\mathrm{Hue} = \mathrm{atan}\left(\frac{b^*}{a^*}\right) \tag{1}$$

where atan() refers to the arctan function. The unit of the resulted hue is given as radian (Loesdau et al., 2014).

The raw reflectance spectra of the core sediments are smooth and featureless. To increase their variance, the FDS (i.e., First-order Derivative Spectrum) was computed, because several characteristic peaks are known to be related to specific mineralogical components in the FDS (e.g., Balsam & Deaton, 1991; Balsam & Wolhart, 1993; Giosan et al., 2002). The FDS was calculated as follows:

$$\mathrm{FDS} = \frac{R_n - R_{(n-1)}}{10} \tag{2}$$

where R_n and $R_{(n\text{-}1)}$ are the nth and $(n-1)$th raw reflectance data, respectively. The denominator 10 refers to the reflectance data measurements at a wavelength step of 10 nm (Balsam & Beeson, 2003). To better understand the paleoceanographic implications of the FDS data set, factor analysis algorithms were applied to the FDS using SPSS software (v. 12). Factor analysis takes m variables and reduces them to n factors. Ideally, n will be substantially less than m. Factor analysis can thus be thought of as summarizing the information in the original variables by combining them into a few weighted averages, which are referred to as factors (Balsam & Wolhart, 1993).

3.2.2. Geochemical Analyses

TC (i.e., total carbon) and TOC (i.e., total organic carbon) measurements were performed on 0.10- and 0.15-g dry bulk sediments sampled at 2-cm intervals. Prior to analysis, the sediments were treated with 40-ml 1.0 N HCl to remove carbonates for TOC and 40-ml distilled water for TC, and then both rinsed with distilled water, dried, and ground. The absolute TOC contents were recalculated to restore the carbonate content using the following equation (Yang et al., 2011):

$$\mathrm{TOC}\% = (12 - \mathrm{TC}\%)/(12 - \mathrm{TOC_m}\%) \times \mathrm{TOC_m}\% \tag{3}$$

where $\mathrm{TOC_m}$ represents the measured results. Replicate analyses (n = 30) of standards of crystine and

sulphanilamide and unknown sediment samples yielded a mean precision of about 0.2% for both TC and TOC tests.

The distribution of Fe, Br, and Ti was determined by an AVAATECH XRF Core Scanner on the split core surface (Wu et al., 2013). Each core segment was covered with a spex certiprep 3525 Ultralens foil (4 μm thick) to protect the probe of the scanner from contamination and was scanned at 1 mA and tube voltages of 10 and 30 kV with counting time of 30 s. The analysis was performed with a sample spot of 1 cm × 1 cm in size and in 1-cm increment. The results are presented as ratios of Fe/Ti, Br/Ti.

3.2.3. Water Content Measurement

Water content was measured immediately after color reflectance measurement at 2-cm intervals as follows: 25–35-g sample taken from the freshly split core was weighed and then dried at 65 °C for 5–7 days. The dried sample was weighed again. Water content was then calculated as follows:

$$\text{Water content (wt.\%)} = (M_w - M_d - M_s)/M_w \times 100\% \tag{4}$$

where M_w and M_d refer to the weights of wet and dried samples, respectively, and M_s is the weight of salt dissolved in the pore water. M_s is assumed to be proportional to the weight of pore water (35:1,000–35) and can be estimated by

$$M_s = (M_w - M_d) \times 35/(1,000\text{–}35) \tag{5}$$

3.2.4. Mineral Analyses

Four Mn-rich samples from intervals of 198–200, 308–310, 392–394, and 496–498 cm representing deglacial deposits were selected to analyze their mineral compositions. Analyses were performed on packed powder mounts of ground, dry bulk sediments using a PANalytical X'Pert PRO diffractometer with CuKa radiation and Ni filter, under a voltage of 45 kV and an intensity of 40 mA. The mounts were scanned continuously from 5° to 70° 2θ with a step size of 0.04 2θ and a count time of 2 s. Identification of mineral species was based on multiple peaks on the derived XRD spectral diagrams.

4. Results

4.1. Mn-Rich Sediment Mineral Composition

Quartz, feldspar, albite, and muscovite are common minerals in the bulk Mn-rich sediments (Figure S1 in the supporting information). Peaks of Mn-bearing mineral phases on the XRD spectral diagrams are also significant, indicating the presence of (amorphormous) Mn-oxides/-hydroxides. No (Mn-bearing) carbonates were detected.

4.2. Downcore Distribution Data

All downcore data from core P1-2 are plotted in Figures 2, 3 against age. According to the core age model, sedimentation rates are variable (Figure 2h), resulting in an uneven distribution of measurements over the past ~520 kyr.

4.2.1. Geochemical Composition

TC content (Figure 2a) is <0.4 wt.% before MIS 6 and varies between 0.4 and 1.8 wt.% thereafter, showing three wide and prominent peaks at MIS 6, late MIS 5, and MIS 3, respectively. TOC content (Figure 2b) varies between 0.2 and 0.6 wt.%. It remains generally low (<0.3 wt.%) before MIS 5 and increases gradually thereafter, lacking a glacial-interglacial variability. A few TOC data points are below the detection limit.

Br/Ti count ratio (Figure 2c) varies between 0.02 and 0.08, with relatively higher values at early MIS 9, MIS 7, and MIS 5. Generally, it lacks variability and shows a slightly increasing trend with decreasing age.

Fe/Ti count ratio (Figure 2d) varies significantly between 9 and 12.5. Higher values occur mainly during glacial periods, particularly during MIS 12, MIS 10, and MIS 2. During interglacial periods, although some small peaks are present, such as during MIS 7 and MIS 5, the ratio generally oscillates near the background level.

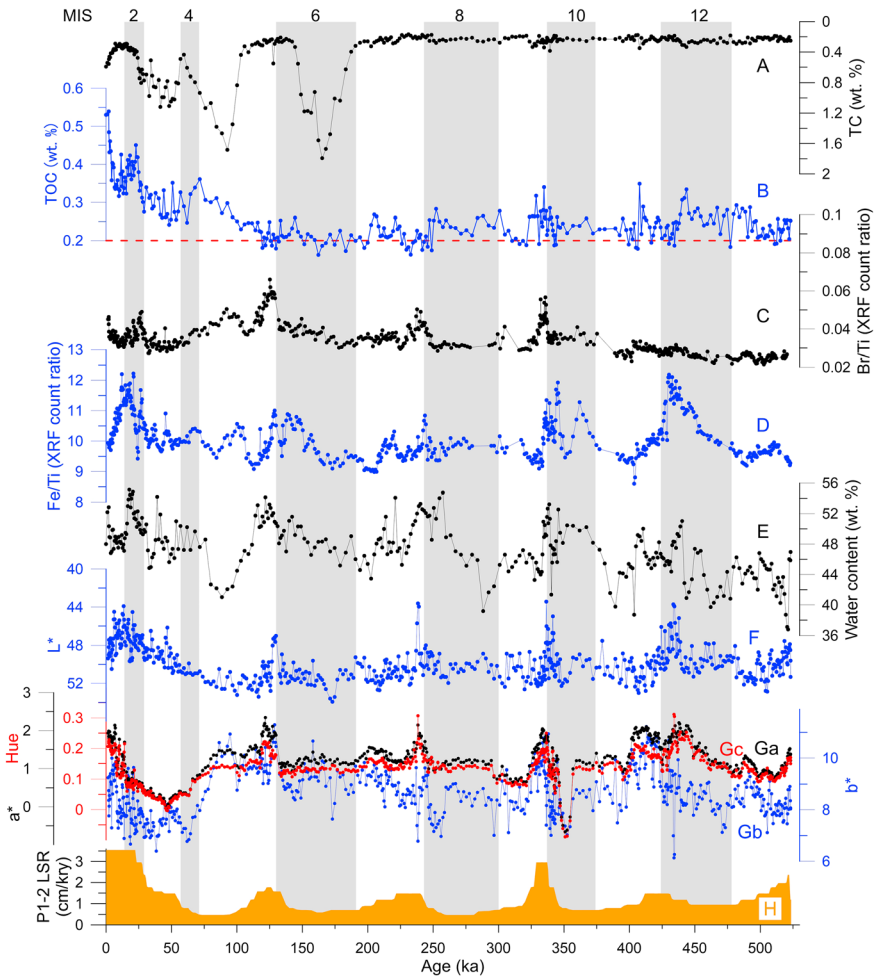

Figure 2. Core P1-2 records over the past 523 ka. (a) Total carbon (TC) content, (b) total organic carbon (TOC) content, (c) X-ray fluorescence (XRF)-scanning-derived Br/Ti count ratio, (d) XRF-scanning-derived Fe/Ti count ratio, (e) Water content, (f) Lightness (L^*), (g-a) a^*, (g-b) b^*, (g-c) Hue, and (h) linear sedimentation rate (LSR). The MIS (i.e., marine isotope stage) are indicated according to Lisiecki and Raymo (2005).

Water content varies cyclically between ~40 and 60 wt.% (Figure 2e). It changes independently against the glacial-interglacial climate cycles shown in the LR04-δ^{18}O stack (Lisiecki & Raymo, 2005) and presents a slightly decreasing trend with increasing age, possibly due to compaction.

4.2.2. Color Data

The Lightness (L^*) in core P1-2 varies between 45 and 60 (Figure 2f). Generally, the L^* values are higher before MIS 4 and gradually decrease to the present. Five additional low spikes occur on the L^* record near MIS 2/1, MIS 6/5, MIS 8/7, MIS 10/9, and MIS 12/11 boundaries.

The a^* (Figure 2g-a) generally ranges from 0 to 2, showing higher values mainly at peak interglacial periods, except for during MIS 12, where it also presents higher values. The b^* (Figure 2g-b) varies between 6 and 12, showing more variability than the a^* record. The hue (Figure 2g-c) generally falls between 0.1 and 0.2, within the red sector of the hue-chroma space (Loesdau et al., 2014). This distribution closely follows the a^* record.

The raw reflectance spectra and the FDSs are shown in Figure 3. Generally, the raw reflectance is relatively low at the short-wavelength end and high at the long-wavelength end (Figure 3b). The FDSs, in contrast, are higher at the short-wavelength band and lower at the long-wavelength band (Figure 3c). Extremely low raw reflectance values occur every ~100 kyr near each glacial-to-interglacial transition zone (Figure 3b), roughly corresponding to the presence of dark brown layers within the core (Figure 3a), and narrow bands of elevated first-order derivatives (Figure 3c).

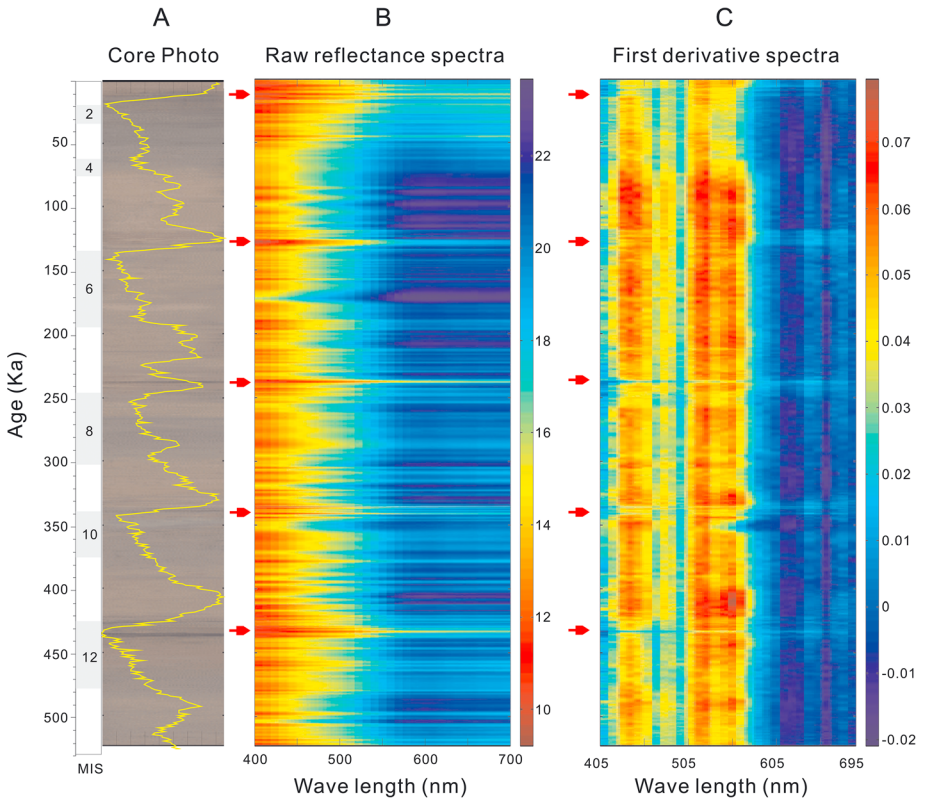

Figure 3. Color reflectance spectra of core P1-2. (a) Photo of the split-core surface, overlapped with the record of LR04 $\delta^{18}O$ stack (Lisiecki & Raymo, 2005; yellow curve). (b) Spectra of the raw color reflectance. (c) First-order Derivative Spectra (FDS) of the sediment color reflectance. Red arrows indicate the dark layers clearly observed in core P1-2. Note that the depth scale of core photo is converted to age scale by interpolation. The MIS (i.e., marine isotope stage) are indicated according to Lisiecki and Raymo (2005).

4.3. Factor Analyses on the FDSs.

The min, max, and mean spectra of the color reflectance of the P1-2 sediments are relatively smooth (Figure 4a). Although different in absolute reflectance levels, they share a similar distribution pattern against the wavelength, with a gradually increasing trend from 400 to 575 nm and a relatively stable interval between 575 to 700 nm. The FDSs show greater variance than the raw reflectance spectra, with two plateaus and generally higher values between 400 and 550 nm, a sharp drop between 550 and 600 nm, and low values thereafter (Figure 4b).

To determine the major factors controlling the sediment color reflectance, we conducted Factor Analyses on the FDS data set. Plot of the communality against the wavelength (Figure 4c) indicates that the 405, 495, and 685–695-nm bands cannot be sufficiently explained with a two- or three-factor model (with communalities <0.6). In a four-factor model instead, these bands are well reproduced (communalities >0.6), while the communalities do not significantly increase further in a five-factor or more factor model. The four factors in the four-factor model all have eigenvalues >1, indicating that each component explains more data variance than any single raw variable within the FDS data set. A cumulative variance of >80% is explained by the four factors (Table S1 and Figure 4d). The goodness-of-fit statistics thus demonstrate that the four-factor model provides the best compromise between the number of factors and the communalities.

After a VARIMAX rotation, the four factors explain 28.5, 25.1, 22.2, and 4.65% of the data variance, respectively (Table S1 and Figure 4d). Loadings for Factor 1 show values gradually increasing from 405 to 585 nm and remaining relatively high thereafter (Figure 4e). Factor 2, in contrast, shows higher values at shorter-wavelength bands and lower values at longer-wavelength bands. Factor 3 shows a major plateau centered

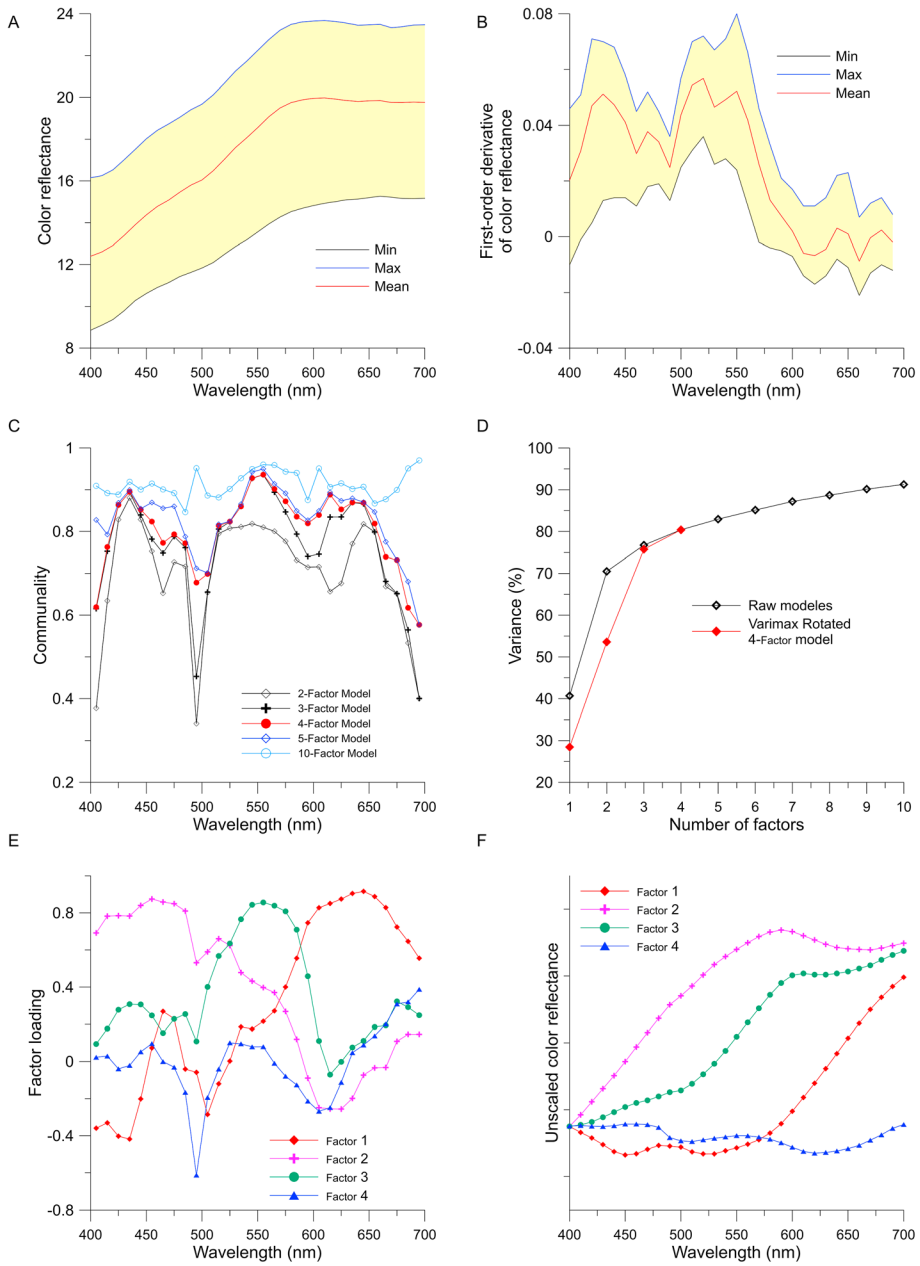

Figure 4. Factor analyses on the color reflectance data set (n = 624) of core P1-2. (a) Summary of the raw spectra of the color reflectance data, including the maximum, mean, and minimum distributions at each wavelength of visible light. (b) Summary of First-order Derivative Spectrum (FDS) of the color reflectance, including the maximum, mean, and minimum distributions at each wavelength of visible light. (c) Communalities of models with 2–10 factors at each wavelength of visible light. The goodness-of-fit statistics suggest that the four-factor model is an adequately reliable choice to accommodate the FDS and thus highlighted (red curve). (d) Cumulative variance explained with increasing factors (2–10). Black curve and circles indicate the original (i.e., unrotated) solutions. Red curve and circles represent the four-factor solution after the VARIMAX rotation. (e) Distribution of factor loadings for the selected model (i.e., four-factor model). (f) Distribution of cumulative factor loadings of the four-factor model. Note that an arbitral reflectance scale is used to simulate the distribution patterns of raw reflectance spectra for the four factors.

at 555 nm and a subsidiary peak at ~445 nm. Factor 4 shows a trough at 445 nm, with the absolute values of the remaining loadings generally <0.4. The reconstructed unscaled reflectance spectra of the four factors are shown in Figure 4f. Factors 1–3 generally show increasing reflectance values as wavelength increases although the slopes are variable. Factor 4, in contrast, shows constantly low reflectance values across the entire range of visible wavelength.

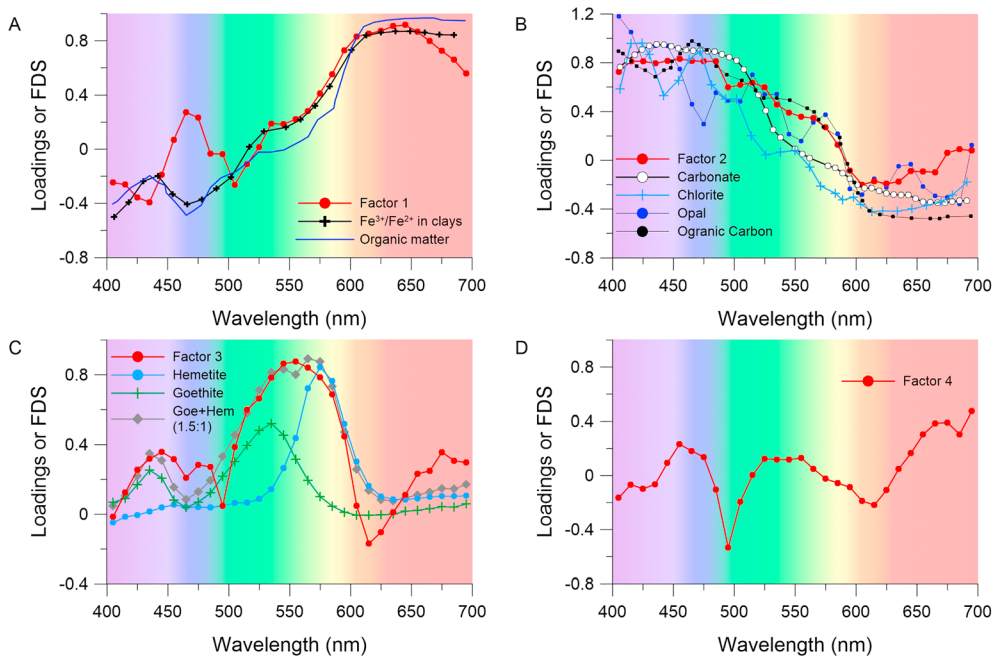

Figure 5. Distributions of the factor loadings of core P1-2 from the selected four-factor model; the data are plotted versus wavelength band of visible light. The factor loadings of known materials are also shown for purpose of verifying our interpretations on the four factors: Fe^{3+}/Fe^{2+} in clays (Giosan et al., 2002) organic matter (Heslop et al., 2007) in (a); carbonate (Giosan et al., 2002), illite and chlorite (Heslop et al., 2007), opal (Clark et al., 2007), organic carbon (Heslop et al., 2007) in (b); and hematite and goethite (0.5 wt. % in a matrix of synthetic Gulf of Mexico sediment; Deaton & Balsam, 1991) in (c). A combination of goethite and hematite FDS curves using a goethite to hematite ratio of 1.5:1 was also shown. Background shades depict the wavelength range of each visible light band.

5. Discussion

This section focuses mainly on interpreting the four extracted color factors from core P1-2 and their associations with paleoceanographic changes in the Southern Ocean. This was approached based mainly on comparing the factor loadings and/or scores with the FDS and/or the temporal changes of already known synthetic or natural materials and sedimentary records. In some cases, however, sediment components do not always influence the color reflectance in a precisely linear way (e.g., Barranco et al., 1989). This is mainly because (1) characteristic peaks on first-order derivative curves of some mineral species (e.g., hematite and goethite) may be offset by varying matrix mineralogy and their concentrations (Balsam & Wolhart, 1993; Deaton & Balsam, 1991) and (2) different mineral species may have similar color reflectance patterns that cannot be distinguished mathematically on their FDS curves (e.g., calcite and opal; Balsam et al., 1999; Giosan et al., 2002). Despite these disadvantages, comparing factor loadings/scores to first-order derivative values and temporal changes of mineral/sediment components is the primary and widely used method for interpreting color factors (e.g., Balsam et al., 2014; Balsam & Wolhart, 1993; Cong et al., 2018; Giosan et al., 2002; Lu et al., 2017; Pan et al., 2014).

5.1. Factor 1 Versus Mn Enrichment and Fe^{3+}/Fe^{2+} Ratio in Clay Minerals

Factor 1 explains 28.5% of the color reflectance data variance (Table S1). We observe higher loadings in the orange to red waveband (600–700 nm) and lower loadings in the purple to blue band (400–500 nm; Figure 5a). Previous studies interpreted FDS components with this distribution pattern to reflect the relative concentrations of organic matter (Balsam & Deaton, 1991), carbonate content (e.g., Balsam et al., 1999), terrigenous content (Harris & Mix, 1999), and Fe^{3+}/Fe^{2+} ratio of the structural iron in clay minerals (Giosan et al., 2002).

In this study, the temporal distribution of the Scores of Factor 1 (SF1) is higher during deglacial periods (Figure 6a). We observe a close coupling between the SF1 and the Mn enrichment records (Figure 6b; Wu et al., 2018). Mn enrichment usually gives the sediment a dark brown color (e.g., Jakobsson et al., 2000). This implies that at least part of the variability of Factor 1 is related to Mn enrichment in the sediment.

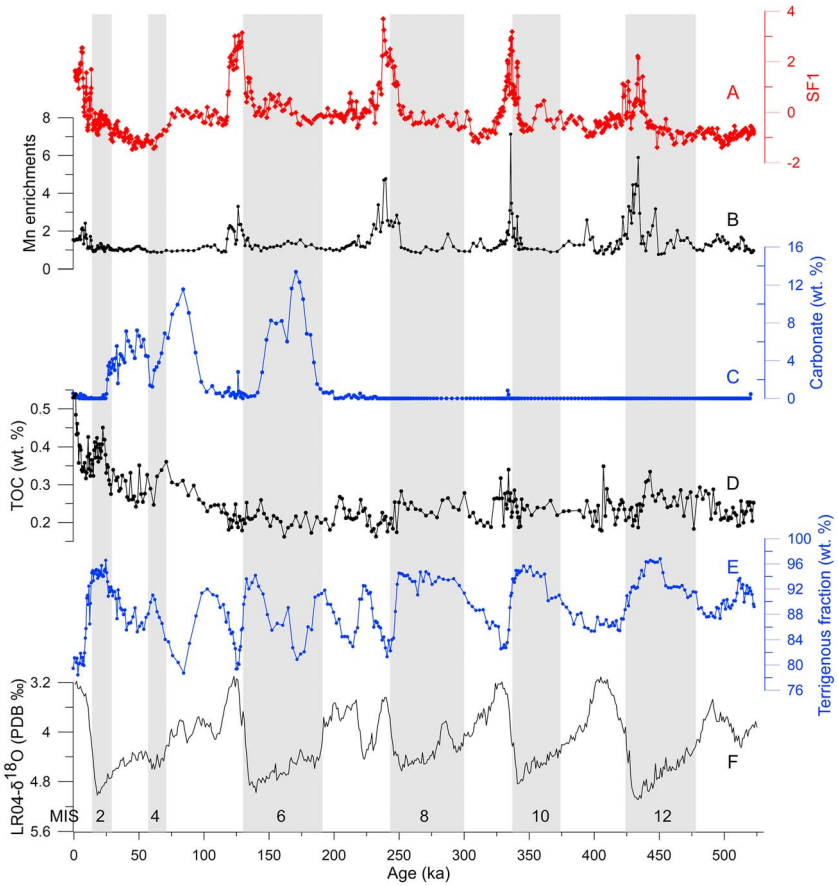

Figure 6. Records used to verify the interpretation on Factor 1. (a) Score of Factor 1 (SF1); (b) Mn enrichment factors (Wu et al., 2018); (c) carbonates content, calculated using (TC-TOC) × 8.33 (wt.%); and (d) TOC content. The dashed line indicates the lower limit of TOC measurement for this study. (e) Terrigenous fraction (wt.%), calculated as 100–Opal (wt.%)–Calcium carbonate (wt.%). Opal data are cited from Wu et al. (2017). (f) LR04 $\delta^{18}O$ stack (Lisiecki & Raymo, 2005). The MIS (i.e., marine isotope stage) are indicated according to Lisiecki and Raymo (2005).

Common Mn-bearing minerals in marine sediments include Mn-oxides/-hydroxides and $(Mn_n, Ca_{1-n})CO_3$ ($0 < n < 1$; Reitz et al., 2006). XRD results from deglacial Mn-rich sediments indicate that Mn-bearing mineral phases are (amorphous) Mn-oxides/-hydroxids. In deep-sea environments, formation of Mn-oxides/-hydroxides must be associated with increased dissolved oxygen. Increased supply of dissolved oxygen results in Mn^{2+} previously dissolved in abyssal waters or sediment pore waters to precipitate at the sediment-water interface (or in sediment at shallow depth below seafloor due to penetration of dissolved oxygen into the sediment; Reitz et al., 2006; Jaccard et al., 2016; Wu et al., 2018). Thus, XRD data support the Mn enrichment record mainly reflecting enhanced abyssal ventilation of the Southern Ocean during recent deglacial periods (Wu et al., 2018), and in turn these deglacial ventilation events have been recorded in the sediment color data.

On the other hand, the distribution pattern of SF1 is basically different from those of the carbonate content (Figure 6c), TOC (Figure 6d), and the terrigenous fraction of the sediment in core P1-2 (Figure 6e), indicating that neither of the above significantly contributes to Factor 1 although their FDSs are similar. Nonetheless, we cannot exclude changes of Fe^{3+}/Fe^{2+} ratio in clays as another chromophore of Factor 1. In fact, elevated oxygen supply to the abyssal waters might also have oxidized part of Fe^{2+}-bearing clay minerals, leading to an increase in the Fe^{3+}/Fe^{2+} ratio in those clays (Giosan et al., 2002). Thus, Factor 1 is interpreted to reflect the integrated signal of relative abundance of Mn enrichment and possibly Fe^{3+}/Fe^{2+} ratio in clays, recording enhanced abyssal ventilation in the Southern Ocean during recent deglacial periods.

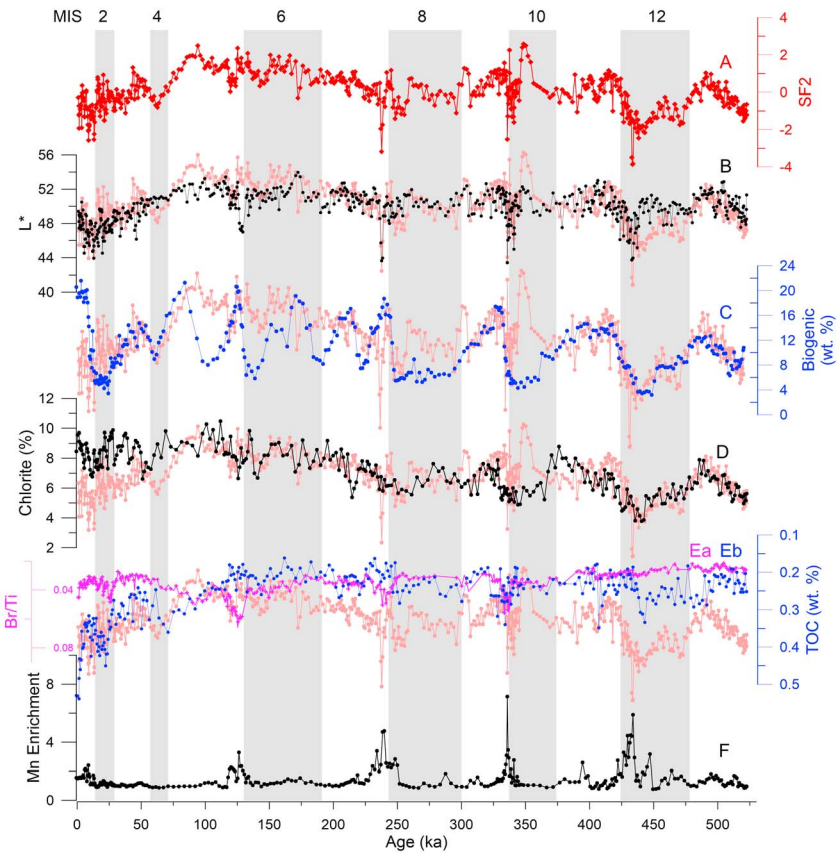

Figure 7. Records used to verify the interpretation on Factor 2. (a) Score of Factor 2 (SF2); (b) L^*; (c) biogenic components, calculated using carbonates + opal (wt.%); (d) Chlorite; (e-a) Br/Ti count ratio; (e-b) TOC (wt. %); and (f) Mn enrichment factor. Records in (b–e) are compared with SF2 shown as soft pink curves. The MIS (i.e., marine isotope stage) are indicated according to Lisiecki and Raymo (2005).

5.2. Factor 2 and Colorless Components

Factor 2 (Figure 5b) explains 25.1% of the total data variance (Table S1). It has higher loadings in the purple to blue band (400–480 nm) and lower loadings in the orange to red band (650–700 nm), showing a distribution pattern inverse to that of Factor 1. Previous studies interpreted this loading distribution pattern as reflecting the presence of carbonates (Giosan et al., 2002), opal (Balsam et al., 1999), illite, chlorite (Heslop et al., 2007), and/or organic matter (Wei et al., 2014) in sediment. Generally, these components are all visually colorless (or lightly colored) and strongly influence sediment lightness (Balsam et al., 1999). Indeed, the score of Factor 2 (SF2; Figure 7a) presents a temporal distribution pattern similar to that of the L^* record (Figure 7b). To identify the chromophores controlling Factor 2, we thus compared SF2 to components that might significantly influence the lightness of the sediment.

In low-latitude oceans, biogenic carbonate is often the dominant factor affecting lightness of marine sediment. In polar regions where preservation of biogenic carbonate is poor, biogenic silica (opal) usually dominates biogenic component in sediment. In P1-2 core sediment, both the carbonate and opal records are positively correlated with SF2 (Table S2), implying that part of the variability of Factor 2 can be explained by content changes in the biogenic components (biogenic carbonate + opal, Figure 7c). A good positive correlation between SF2 and the chlorite percentage record (<2-μm fraction; Figure 7d; Wu, 2017) was observed as well (Table S2), indicating that chlorite may be another important factor explaining Factor 2. However, the correlation between SF2 and illite, which also has a FDS of Factor 2 style (Heslop et al., 2007), is insignificant (Table S2).

Chlorite and illite are respectively the most subordinate (with a mean of ~8%) and the most abundant (~57%) clay mineral species in the core sediment (Wu, 2017). Their disproportional contributions to Factor 2

indicate that sediment color is not necessarily determined by components with high abundance. This is also well reflected in the correlation between the TOC (Figure 7b) and SF2.

We suggest that organic carbon is likely responsible for part of SF2 variability as well, as a so-called *volume effect* exists for organic carbon in marine sediments (Balsam et al., 1999). This occurs because density of organic matter is so low that even a small weight percent fraction of organic matter can occupy a relatively large area on the sediment surface, thereby reducing reflectance of sediment (Balsam & Wolhart, 1993; Wei et al., 2014).

This volume effect may also exist in our records. We notice that although TOC content (Figure 7e-b) is generally low, the gradual increase in TOC after late MIS 5 is well coupled with the decrease in SF2. This provides complementary explanation for the decrease in values of SF2 during this time period when the coupling between biogenic components/chlorite and SF2 is reduced.

It is also noteworthy that Br/Ti record (Figure 7e-a) does not covary with TOC record in this study. In fact, TOC record reflects organic carbon content of both marine and terrigenous origins, while Br/Ti only reflects that of marine origin (Mayer et al., 2007; Ziegler et al., 2013). In particular, during late MIS 5 to MIS 1, TOC is significantly higher than Br/Ti, which generally fluctuates in its background level, implying that terrigenous organic carbon dominates the sedimentary TOC during this interval.

Low TOC in our core sediment throughout glacial-interglacial changes is consistent with low TOC records from Ocean Drilling Program (ODP) sites 1167 and 1165 drilled in Prydz Bay area (Shipboard-Scientific-Party, 2000) and may be because (1) bottom water in the study area is oxygen rich, especially during interglacial periods, leading to high rate of remineralization of organic carbon (Pilskaln et al., 2004) and (2) low sedimentation (~1 cm/kyr) prolongs exposure of organic carbon at sediment-water interface. In any case, the environmental setting allows only the refractory fraction of organic carbon being preserved. The coupling between TOC and SF2 after MIS 5 thus indicates that SF2 is significantly influenced by refractory organic carbon of terrigenous origin.

Besides the above, we also suggest that Mn-oxides/-hydroxides (Figure 7f) may influence Factor 2 as well due to its dark brown color (Deaton & Balsam, 1991), because we observed that low SF2 values correspond well with high Mn enrichment factors near MIS 12/11, MIS 10/9, and MIS 8/7 boundaries when the values of Mn enrichment peaks exceed ~3.

Therefore, Factor 2 is a complex factor that mainly reflects relative changes in total biogenic components and chlorite percentage but might be also influenced by other colorless components in the sediment, such as refractory terrigenous organic carbon and Mn-oxides/-hydroxides.

5.3. Factor 3 and Hematite and Goethite

Factor 3 explains 22.2% of the data variance (Table S1). Its loading curve is bimodal, with a high plateau between 505 and 605 nm and a second peak between 405 and 495 nm (Figure 5c). This distribution pattern is similar to goethite and hematite curves, which are common minerals in variable environmental settings (e.g., Balsam et al., 2014; Barranco et al., 1989; Deaton & Balsam, 1991; Pan et al., 2014; Wei et al., 2014). The FDS curve of goethite is characterized by a major peak centered at 535 nm and a second peak at ~435 nm, while that of hematite is unimodal, with only one peak centered at 565–575 nm (Balsam et al., 2014; Deaton & Balsam, 1991). The combination of goethite plus hematite FDS curves reproduces the characteristic peaks on the loading curve of Factor 3 very well (in this case, using a goethite to hematite ratio of 1.5:1). Factor 3 thus was interpreted as mainly representing the relative abundance of hematite and goethite assemblage in the sediments. Higher (lower) SF3 values (Figure 8a) indicate higher (lower) relative concentrations of hematite plus goethite assemblage (respectively). The interpretation is supported by the correspondence between the SF3 and the Hue (Figure 8B) records, because hematite and goethite are rich in Fe^{3+} and are the common minerals that contribute a reddish hue to sediments (e.g., Balsam & Wolhart, 1993; Cong et al., 2018; Giosan et al., 2002; Heslop et al., 2007; Lu et al., 2017; Pan et al., 2014; Reynolds et al., 2014; Wei et al., 2014; Yang & Ding, 2003).

The SF3 displays some similarities with the Fe/Ti record (Figure 8d) as well. The Fe/Ti record is used here to characterize the excess Fe that is not associated with aluminosilicates, for example, hematite, goethite, and magnetite etc (Martínez-Garcia et al., 2011). The similarities between the SF3 and the Fe/Ti might result

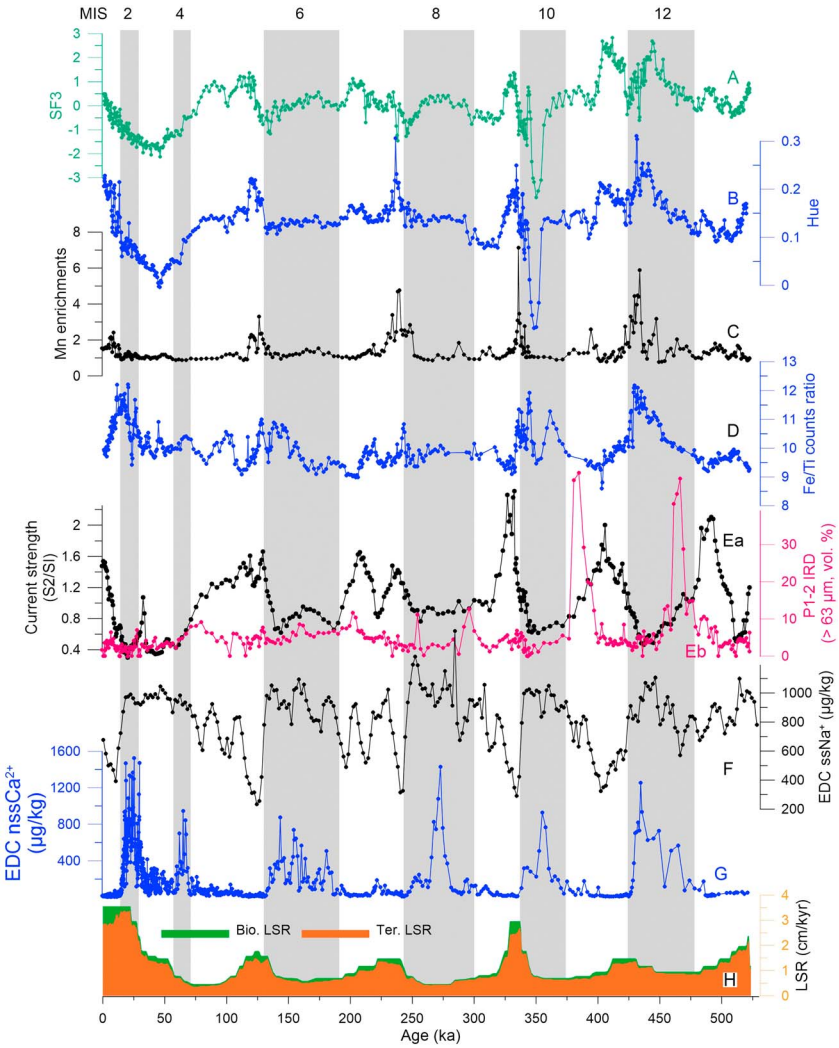

Figure 8. Records used to support the interpretation on Factor 3. (a) Scores of Factor 3; (b) Hue; (c) Mn enrichments (Wu et al., 2018); (d) XRF core-scanner-derived Fe/Ti ratio; and (e-a) grain size inferred local currents (Wu et al., 2018). Higher (lower) values indicate stronger (weaker) current (respectively). S1 and S2 refer to sensitive grain size classes 1 and 2, respectively; (e-b) > 63-μm fraction of the nonbiogenic sediments (Wu et al., 2018). It was measured by Laser Particle Sizer and used here to indicate IRD delivery to the core site. (f) EDC $ssNa^{+}$, representative of past winter sea ice extent around Antarctica. Higher (lower) values indicate more narrow (wider) sea ice extent (respectively). (g) EDC $nssCa^{2+}$, representative of past dust flux to the Antarctic region. (h) LSR, linear sedimentation rate of core P1-2. Bio. LSR and Ter. LSR refer to partial sedimentation rate of biogenic components and nonbiogenic components, respectively. Bio. LSR = LSR × (Opal wt.% + carbonates wt.%) and Ter. LSR = LSR × (1-Bio. LSR). The MIS (i.e., marine isotope stage) are indicated according to Lisiecki and Raymo (2005).

from the relative concentration changes in hematite plus goethite assemblage that are consistent with the *Fe-related* interpretation of Factor 3. However, the Fe/Ti record may have also been complicated by changes in other Fe-bearing minerals. For example, there are a series of glacial peaks on the Fe/Ti curve that are not shown on the SF3 curve, such as those during MIS 12, MIS 10, and MIS 2. These peaks might be more consistent with contemporarily elevated dust flux to the Antarctic region (EPICA-Community-Members, 2004; Figure 8g).

However, our study area is close to the Antarctic continent and terrigenous input is dominated by proximal sources (e.g., Ehrmann et al., 1992; Passchier, 2011; Borchers et al., 2011). In addition, the Prydz Bay region is located far from sources of dust from Patagonia, South America (Li et al., 2008). Therefore, dust deposits at our core site should be minimal and diluted by terrigenous sediments from the Antarctic continent. This is supported by differences in clay mineralogy between the Prydz Bay region and the Patagonia dust source

area. Clay minerals from the Patagonia dust source area are dominated by smectite and chlorite (Diekmann et al., 1996, 1999; Gaiero et al., 2004). In our study area, previous studies show that the clay mineral assemblage is dominated by illite, with only minor chlorite (~8%) and significant kaolinite/smectite reworked from old successions on Antarctica during cold periods when dust input was high (Ehrmann et al., 2003; Junttila et al., 2005; Borchers et al., 2011, 2016; Wu, 2017). Thus, the additional Fe/Ti peaks during glacial periods are more likely introduced from the Antarctica continent.

Hematite and goethite in abyssal ocean sediments are derived ultimately from adjacent continents (Balsam et al., 1995; Barranco et al., 1989; Giosan et al., 2002), because these minerals primarily form under subaerial conditions (Ao et al., 2011; Balsam & Wolhart, 1993). Hematite forms in a warm and dry environment, while a cold and humid climate favors formation of goethite (Ao et al., 2011; Reynolds et al., 2014). The hematite to goethite ratio is frequently used as an indicator of climate alternations (Ao et al., 2011; Balsam & Wolhart, 1993). The two minerals possess different FDS distributions (Barranco et al., 1989; Deaton & Balsam, 1991; Wei et al., 2014). In our records, however, these two minerals cannot be mathematically separated using the factor analysis technique, suggesting that their concentrations were not controlled by production under different climate regimes but likely by redistribution from old successions containing both minerals.

SF3 generally shows higher values during peak interglacial intervals after peaks in Mn enrichment (Figure 8c) when strength of local currents (Figure 8e-a) was strong (Wu et al., 2018), but ice-rafted debris (IRD) delivery (Figure 8e-b; Wu et al., 2018), sea ice extent (Figure 8f), and dust input (Figure 8g; EPICA-Community-Members, 2004) were generally low. This suggests that transportation by currents might be responsible for the hematite and goethite assemblage in the core sediments, while IRD delivery, sea ice entrainment, and dust input might have played an insignificant role. This is further supported by the close coupling between the SF3 record (Figure 8a) and the tuned sedimentation rate record (Figure 8h).

The total sedimentation rate can be divided into the biogenic and the terrigenous parts. Calculations indicate that elevated export production only accounts for a small fraction of elevated total sedimentation rate during deglacial and early interglacial periods, and the major part of the total sedimentation rate must be contributed from the terrigenous input, which likely corresponds to higher sediment transport efficiency from the adjacent continent (e.g., Borchers et al., 2011; Ehrmann et al., 1992; Passchier, 2011). The high peak in SF3 during MIS 12, however, might result from a provenance change for reasons that need to be studied further.

5.4. Factor 4 and Water Content

Factor 4 (Figure 5d) only accounts for a small fraction of the data variance (~4%, Table S1). It has a low and flat distribution pattern of factor loadings. This factor was seldom found in previous work. Here we correlate it attentively to water content in the core sediments because (1) the integrated loadings of this factor show a low (relative to other factors) and flat pattern generally parallel with the wavelength axis (Figure 4f), suggesting that the reflectance is evenly distributed and generally low against the whole band of visible light, and this feature is similar to impact of water on sediment reflectance; that is, adding water to sediments will significantly reduce reflectance of the sediments on the whole visible light band (Balsam et al., 1998). Particularly, the unscaled reflectance of Factor 4 is generally lower at the red (right) end than at the violet (left) end (Figure 4f), consistent with observations that the greatest amount of darkening takes place at the red end of reflectance spectrum when water is added to sediments (Balsam et al., 1998); (2) the temporal change of the Scores of Factor 4 (SF4, Figure 9a) is very similar to that of measured water content in the sediments (Figure 9b and Table S3).

Water in sediments can occur as interstitial water, absorbed water, interlayer water, structure water, and bound water (e.g., Bauer & Vennemann, 2014; Klute, 1986). In this study, under a heating temperature of 65 °C, only the mobile waters were removed. Therefore, the water content measurements (Figure 9b) and Factor 4 only record the loss of these mobile waters.

In the Southern Ocean, previous studies showed that water content records of diatom-rich sediments display similar temporal changes with their opal content record (e.g., Hillenbrand et al., 2009; Huang, 2017; Weber et al., 2012), because diatom remains dominate the water-bearing components of those sediments ($SiO_2 \cdot nH_2O$). In our record, a low but significant positive correlation exists between the content records of opal (Figure 9c) and water (Table S3), confirming the influence of opal deposits on the sediment-water

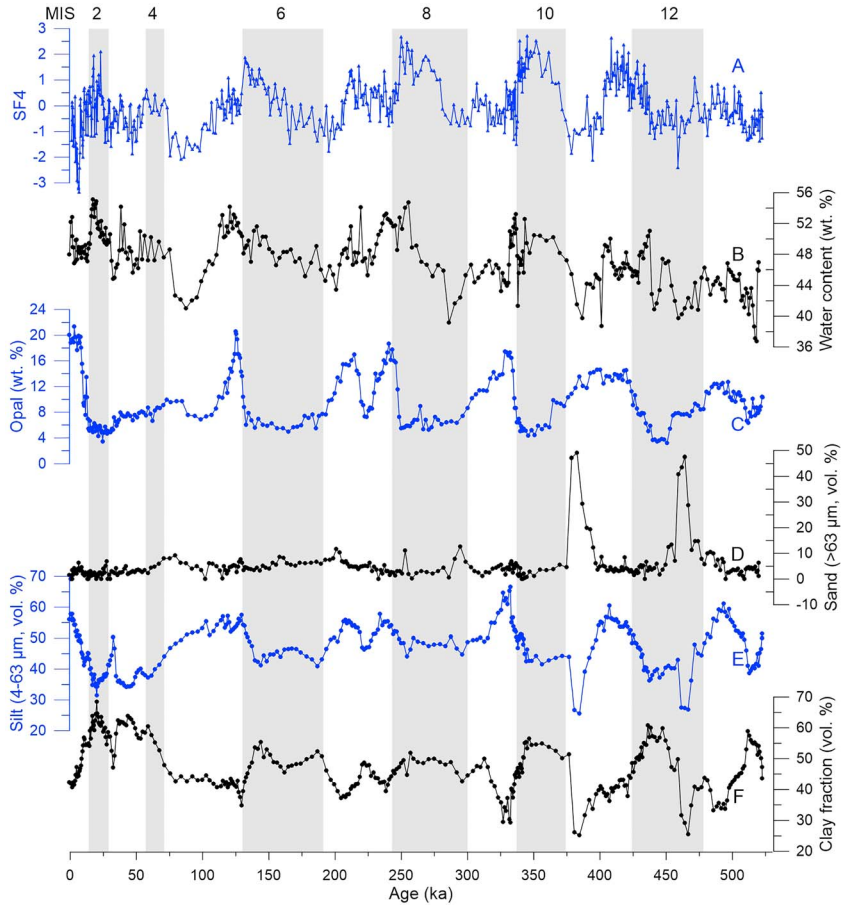

Figure 9. Records used to support the interpretation of Factor 4. (a) Scores of Factor 4 (SF4), (b) water content, and (c) opal content (Wu et al., 2017), (d–f) sand, silt, and clay volume fractions of the nonbiogenic sediments derived from Laser Particle Sizer (Wu et al., 2018). The MIS (i.e., marine isotope stage) are indicated, shown with the LR04 $\delta^{18}O$ stack (Lisiecki & Raymo, 2005).

content. However, opal content is generally low, varying between 3.21 and 21.3 wt.% with a mean of 9.7 wt. % (Wu et al., 2017), resulting in the low correlation with the water content.

We also notice that the water content is negatively correlated with the sand fraction (Figure 9d) and positively correlated with the clay fraction (Figure 9f and Table S3). We suggest three reasons for this observation: (1) The sand fraction is dominated by quartz, dark minerals, and rock fragments that are all dense materials with little water content. Clay-sized sediments, in contrast, contain large fraction of layered, water-bearing clay minerals (Klute, 1986). (2) The porosity of clay-rich sediment is higher than that of sand, although the space of an individual pore between sand-sized grains is larger than that between clay-sized grains. (3) Pore space between clay-sized grains is filled mainly by pore water, while pore space between sand-sized grains is filled mostly by fine sediments that may be water free. (3) Larger pore space between sand-sized grains also results in higher dewatering rate in sand-rich layer than in clay-rich layer during coring, splitting, and sampling. Within the silt fraction (Figure 9f), correlation to water content is insignificant (Table S3) because of its intermediate grain size between sand and clay, thus incorporating both water-bearing and water-free factors within this grain size range.

5.5. Robustness of the Color Factors

The four factors derived from sediment color reflectance data of core P1-2 can be correlated to real sediment components, thus containing useful information on paleoceanographic evolution of the Southern Ocean. However, to be cautious, the robustness of these color factors still need to be evaluated as no similar work done previously in the Southern Ocean.

For this purpose, we applied the same FDS and factor analysis algorithms on sediment cores P1-3 and P4-1 as on core P1-2. Generally, the three cores were retrieved from the same sedimentary environment and are expected to record identical information on regional paleoenvironmental change (Wu et al., 2017). Thus, results of factor analysis on color reflectance data from these cores are also expected to be similar if those color factors are robust statistically.

The factor analysis results show that four-factor models are the best for cores P1-3 and P4-1 as well (Figures 2a and 2b). Further, intercore comparisons indicate that changes of color factors in the three cores are rather consistent. Namely, not only factor loading distributions (Figures S2c–S2f) but also temporal change patterns of factor scores of the four factors (Figure S3) are respectively similar in the three cores. Although minor difference exists possibly due to difference of local environment and/or uncertainties of calculation, the general consistency of the factor analysis results between the three cores supports the statistical robustness of these derived color factors.

In summary, this study demonstrates that visible light reflectance of sediments from the Southern Ocean might register useful and possibly important information on local paleoenvironmental evolution and thus worth to be studied and applied in future work. Specifically, Factor 1 in this study, with information on abyssal ventilation, is expected to be found in sediments from much wider Antarctic marginal seas, because enhanced abyssal ventilation is one of the most prominent features of the deglacial Southern Ocean, directly linking to past changes in atmospheric CO_2 (Jaccard et al., 2016). More work should be involved to further confirm the validity and applicability of such color factor. Such work is especially beneficial for studies on those long sedimentary archives (e.g., International Ocean Discovery Program cores), as easy-to-be-obtained, inexpensive, high-resolution, and informative proxies are extremely attractive.

6. Conclusions

We investigated the color reflectance data of sediment cores ANT30/P1-02, ANT30/P1-03, and ANT29/P4-01 retrieved off Prydz Bay, East Antarctica, using FDS and factor analysis algorithms to understand the correlations between the sediment color and the sediment compositions. TC content, TOC content, water content, XRD mineral compositions, and XRF-scanning-derived Fe/Ti and Br/Ti count ratios of core P1-2 sediments were measured to support this study. Major conclusions are drawn as follows:

1. The FDS data calculated from the raw color reflectance data of the studied core sediments can be adequately explained by a four-factor model using factor analysis algorithms. The four factors explain >80% of total data variance. These factors are robust and can be correlated to real compositions of the core sediments and thus provide useful core parameters and paleoenvironmental proxies.
2. Factor 1 explains the Mn enrichments and possibly Fe^{3+}/Fe^{2+} ratio of the structural iron in clay minerals, recording enhanced abyssal ventilation during recent deglacial periods in the Southern Ocean.
3. Factor 2 is a complex factor mainly reflecting reflectance of the biogenic components plus chlorite in the core sediment. But refractory organic carbon and Mn-oxides/-hydroxides may also significantly contribute to this factor.
4. Factor 3 explains the relative concentration changes of hematite and goethite assemblage in the sediment. It shows generally higher values during interglacial periods and lower ones during glacial periods, generally coupled with temporal changes in the sedimentation rate. Interglacial enrichment of hematite and goethite assemblage is due to enhanced transport and deposition of sediment of local origin by oceanic currents.
5. Factor 4 was correlated to water content of the core sediment. Opal content and clay-sized fraction are positively correlated with the water content, while sand-sized and silt-sized fractions are either negatively correlated or noncorrelated with the water content, suggesting that opal content and sediment grain size compositions affect the sediment-water content significantly.

Acknowledgments
We sincerely thank the reviewers for their constructive comments and suggestions that helped to improve the manuscript significantly. Thanks also go to Prof. Gert J. Delange, who read and commented an early version of this manuscript, and Dr. Pingyuan Li and Dr. Guoyong Zhao, who kindly helped conducting the XRD experiment. Prof. Ellen A. Cowan helped rephrasing the final version of the manuscript and is sincerely thanked here. We thank the 29th and 30th Chinese Antarctic Expedition cruise members for retrieving the sediments. This work is jointly supported by Chinese National Natural Science Foundation and China Postdoctoral Science Foundation (grants 41806223, 2018 M632158, 41776191, and 41676191). The data sets analyzed during the current study can be downloaded as the supporting information.

References

Anderson, R. F., Ali, S., Bradtmiller, L. I., Nielsen, S. H. H., Fleisher, M. Q., Anderson, B. E., & Burckle, L. H. (2009). Wind-driven upwelling in the Southern Ocean and the deglacial rise in atmospheric CO_2. *Science*, *323*(5920), 1443–1448. https://doi.org/10.1126/science.1167441

Ao, H., Dekkers, M. J., Qin, L., & Xiao, G. (2011). An updated astronomical timescale for the Plio-Pleistocene deposits from South China Sea and new insights into Asian monsoon evolution. *Quaternary Science Reviews*, *30*(13-14), 1560–1575. https://doi.org/10.1016/j.quascirev.2011.04.009

Balsam, W., Damuth, J. E., & Deaton, B. (2007). Marine sediment components: Identification and dispersal assessed by diffuse reflectance spectrophotometry. *International Journal of Environment and Health*, *1*(3), 403–426. https://doi.org/10.1504/IJENVH.2007.017869

Balsam, W., & Deaton, B. (1991). Sediment dispersal in the Atlantic Ocean: Evaluation by visible light spectra. *Reviews in Aquatic Science*, *4*, 411–447.

Balsam, W. L., & Beeson, J. P. (2003). Sea-floor sediment distribution in the Gulf of Mexico. *Deep Sea Research Part I: Oceanographic Research Papers*, *50*(12), 1421–1444. https://doi.org/10.1016/j.dsr.2003.06.001

Balsam, W. L., & Damuth, J. E. (2000). Further investigations of shipboard vs. shore-based spectral data: Implications for interpreting Leg 164 sediment composition. In C. K. Paull, R. Matsumoto, P. J. Wallace, & W. P. Dillon (Eds.), *Proceedings of the Ocean Drilling Program* (Vol. 164, pp. 313–324).

Balsam, W. L., Damuth, J. E., & Schneider, R. R. (1997). Comparison of shipboard vs. shore-based spectral data from Amazon Fan cores: Implications for interpreting sediment composition. Proc. ODP, Sci. Results 155, 193–215.

Balsam, W. L., & Deaton, B. C. (1996). Determining the composition of Late Quaternary marine sediments from NUV, VIS, and NIR diffuse reflectance spectra. *Marine Geology*, *134*(1-2), 31–55. https://doi.org/10.1016/0025-3227(96)00037-0

Balsam, W. L., Deaton, B. C., & Damuth, J. E. (1998). The effects of water content on diffuse reflectance spectrophotometry studies of deep-sea sediment cores. *Marine Geology*, *149*(1-4), 177–189. https://doi.org/10.1016/S0025-3227(98)00033-4

Balsam, W. L., Deaton, B. C., & Damuth, J. E. (1999). Evaluating optical lightness as a proxy for carbonate content in marine sediment cores. *Marine Geology*, *161*, 141–153. https://doi.org/10.1016/S0025-3227(99)00037-7

Balsam, W. L., Ji, J., Renock, D., Deaton Bobby, C., & Williams, E. (2014). Determining hematite content from NUV/Vis/NIR spectra: Limits of detection. *American Mineralogist*, *99*(11-12), 2280–2291. https://doi.org/10.2138/am-2014-4878

Balsam, W. L., Otto-Bliesner, B. L., & Deaton, B. C. (1995). Modern and Last Glacial Maximum eolian sedimentation patterns in the Atlantic Ocean interpreted from sediment iron oxide content. *Paleoceanography*, *10*(3), 493–507. https://doi.org/10.1029/95PA00421

Balsam, W. L., & Wolhart, R. (1993). Sediment dispersal in the Argentine Basin: Evidence from visible light spectra. *Deep Sea Research Part II: Topical Studies in Oceanography*, *40*(4-5), 1001–1031. https://doi.org/10.1016/0967-0645(93)90046-P

Barranco, F. T., Balsam, W. L., & Deaton, B. C. (1989). Quantitative reassessment of brick red lutites: Evidence from reflectance spectrophotometry. *Marine Geology*, *89*(3-4), 299–314. https://doi.org/10.1016/0025-3227(89)90082-0

Bauer, K., & Vennemann, W. (2014). Analytical methods for the measurement of hydrogen isotope composition and water content in clay minerals by TC/EA. *Chemical Geology*, *363*, 229–240. https://doi.org/10.1016/j.chemgeo.2013.10.039

Billmeyer, F. W., & Saltzman, M. (1981). The coloring of materials in industry. In F. W. Billmeyer & M. Saltzman (Eds.), *Principles of color technology* (pp. 133–172). New York: Wiley.

Bindoff, N. L., Rosenberg, M. A., & Warner, M. J. (2000). On the circulation and water masses over the Antarctic continental slope and rise between 80 and 150°E. *Deep Sea Research Part II: Topical Studies in Oceanography*, *47*(12-13), 2299–2326. https://doi.org/10.1016/S0967-0645(00)00038-2

Borchers, A., Dietze, E., Kuhn, G., Esper, O., Voigt, I., Hartmann, K., & Diekmann, B. (2016). Holocene ice dynamics and bottom-water formation associated with Cape Darnleypolynya activity recorded in Burton Basin, East Antarctica. *Marine Geophysical Research*, *37*(1), 49–70.

Borchers, A., Voigt, I., Kuhn, G., & Diekmann, B. (2011). Mineralogy of glaciomarine sediments from the Prydz Bay–Kerguelen region: Relation to modern depositional environments. *Antarctic Science*, *23*(2), 164–179. https://doi.org/10.1017/S0954102010000830

Clark, R. N., Swayze, G. A., Wise, R., Livo, E., Hoefen, T., Kokaly, R., & Sutley, s. j. (2007). USGS digital spectral library splib06a. US Geol. Surv. Digital Data Ser., 231. Retrieved from http://speclab.cr.usgs.gov/spectral.lib06/ds231/index.html#SMSE

Cong, Z., Gao, S., Zhao, W., Wang, X., Wu, G., Zhang, Y., et al. (2018). Iron oxides in the cryoconite of glaciers on the Tibetan Plateau: Abundance, speciation and implications. *The Cryosphere*, *12*(10), 3177–3186. https://doi.org/10.5194/tc-12-3177-2018

Cooper, A.K., O'Brien, P.E., 2004. Leg 188 synthesis: Transitions in the glacial history of the Prydz Bay region, East Antarctica, from ODP drilling. Proc. ODP, Sci. Results 188, 1-42.

Deaton, B. C., & Balsam, W. L. (1991). Visible spectroscopy: A rapid method for determining hematite and goethite concentration in geological materials. *Journal of Sedimentary Petrology*, *61*(4), 628–632. https://doi.org/10.1306/D4267794-2B26-11D7-8648000102C1865D

Debret, M., Desmet, M., Balsam, W., Copard, Y., Francus, P., & La, C. (2006). Spectrophotometer analysis of Holocene sediments from an anoxic fjord: Saanich Inlet, British Columbia, Canada. *Marine Geology*, *229*(1-2), 15–28. https://doi.org/10.1016/j.margeo.2006.01.005

Debret, M., Sebag, D., Desmet, M., Balsam, W., Copard, Y., Mourier, B., et al. (2011). Spectrocolorimetric interpretation of sedimentary dynamics: The new "Q7/4 diagram". *Earth-Science Reviews*, *109*(1-2), 1–19. https://doi.org/10.1016/j.earscirev.2011.07.002

Diekmann, B., Kuhn, G., Mackensen, A., Petschick, R., Fütterer, D. K., Gersonde, R., et al. (1999). Kaolinite and chlorite as tracers of modern and Late Quaternary deep water circulation in the South Atlantic and the adjoining Southern Ocean. In G. Fischer & G. Wefer (Eds.), *Use of proxies in paleoceanography: Examples from the South Atlantic* (pp. 285–313). Berlin Heidelberg, Berlin, Heidelberg: Springer. https://doi.org/10.1007/978-3-642-58646-0_11

Diekmann, B., Petsehick, R., Gingele, F. X., Fütterer, D. K., Abelmann, A., Brathauer, U., et al. (1996). Clay mineral fluctuations in Late Quaternary sediments of the southeastern South Atlantic: Implications for past changes of deep water advection. In G. Wefer, W. H. Berger, G. Siedler, & D. J. Webb (Eds.), *The South Atlantic: Present and Past Circulation* (pp. 621–644). Berlin Heidelberg, Berlin, Heidelberg: Springer. https://doi.org/10.1007/978-3-642-80353-6_31

Ehrmann, W., Bloemendal, J., Hambrey, M. J., McKelvey, B., &Whitehead, J. (2003). Variations in the composition of the clay fraction of the Cenozoic Pagodroma Group, East Antarctica: Implications for determining provenance. *Sedimentary Geology*, *161*(1–2), 131–152.

Ehrmann, W. U., Melles, M., Kuhn, G., & Grobe, H. (1992). Significance of clay mineral assemblages in the Antarctic Ocean. *Marine Geology*, *107*(4), 249–273. https://doi.org/10.1016/0025-3227(92)90075-S

EPICA-Community-Members (2004). Eight glacial cycles from an Antarctic ice core. *Nature*, *429*(6992), 623–628. https://doi.org/10.1038/nature02599

Forsberg, C. F., Florindo, F., Grützner, J., Venuti, A., & Solheim, A. (2008). Sedimentation and aspects of glacial dynamics from physical properties, mineralogy and magnetic properties at ODP Sites 1166 and 1167, Prydz Bay, Antarctica. *Palaeogeography, Palaeoclimatology, Palaeoecology*, *260*(1-2), 184–201. https://doi.org/10.1016/j.palaeo.2007.08.022

Gaiero, D. M., Depetris, P. J., Probst, J. L., Bidart, S. M., & Leleyter, L. (2004). The signature of river- and wind-borne materials exported from Patagonia to the southern latitudes: A view from REEs and implications for paleoclimatic interpretations. *Earth & Planetary Science Letters*, *219*(3-4), 357–376. https://doi.org/10.1016/s0012-821x(03)00686-1

Giosan, L., Flood, R. D., & Aller, R. C. (2002). Paleoceanographic significance of sediment color on western North Atlantic drifts: I. Origin of color. *Marine Geology*, *189*(1-2), 25–41. https://doi.org/10.1016/S0025-3227(02)00321-3

Grützner, J., Rebesco, M., Cooper, A., Forsberg, C., Kryc, K., & Wefer, G. (2003). Evidence for orbitally controlled size variations of the East Antarctic Ice Sheet during the late Miocene. *Geology*, *31*(9), 777–780. https://doi.org/10.1130/G19574.1

Harris, S. E., & Mix, A. C. (1999). Pleistocene precipitation balance in the Amazon Basin recorded in deep sea sediments. *Quaternary Research*, *51*(1), 14–26. https://doi.org/10.1006/qres.1998.2008

Heslop, D., Dobeneck, T.v., & Höcker, M. (2007). Using non-negative matrix factorization in the "unmixing" of diffuse reflectance spectra. *Marine Geology*, *241*(1-4), 63–78. https://doi.org/10.1016/j.margeo.2007.03.004

Hillenbrand, C. D., Kuhn, G., & Frederichs, T. (2009). Record of a Mid-Pleistocene depositional anomaly in West Antarctic continental margin sediments: An indicator for ice-sheet collapse? *Quaternary Science Reviews*, *28*(13-14), 1147–1159. https://doi.org/10.1016/j.quascirev.2008.12.010

Huang, M. (2017). Paleoceanographic changes since late MIS 3 in the Joides Trough on the northwestern Ross Sea continental shelf, Antarctica (Master's thesis) (pp. 31–37. China: Tongji University.

Jaccard, S., Hayes, C. T., Martínez-García, A., Hodell, D., Anderson, R. F., Sigman, D., & Haug, G. (2013). Two modes of change in Southern Ocean productivity over the past million years. *Science*, *339*(6126), 1419–1423. https://doi.org/10.1126/science.1227545

Jaccard, S. L., Galbraith, E. D., Martínez-García, A., & Anderson, R. F. (2016). Covariation of deep Southern Ocean oxygenation and atmospheric CO_2 through the last ice age. *Nature*, *530*(7589), 207–210. https://doi.org/10.1038/nature16514

Jakobsson, M., Løvlie, R., Al-Hanbali, H., Arnold, E., Backman, J., & Mörth, M. (2000). Manganese and color cycles in Arctic Ocean sediments constrain Pleistocene chronology. *Geology*, *28*(1), 23–26. https://doi.org/10.1130/0091-7613(2000)28<23:MACCIA>2.0.CO;2

Ji, J., Balsam, W., Chen, J. U., & Liu, L. (2002). Rapid and quantitative measurement of hematite and goethite in the Chinese loess-paleosol sequence by diffuse reflectance spectroscopy. *Clays and Clay minerals*, *50*(2), 208–216. https://doi.org/10.1346/000986002760832801

Ji, J., Shen, J., Balsam, W., Chen, J., Liu, L., & Liu, X. (2005). Asian monsoon oscillations in the northeastern Qinghai–Tibet Plateau since the late glacial as interpreted from visible reflectance of Qinghai Lake sediments. *Earth and Planetary Science Letters*, *233*(1-2), 61–70. https://doi.org/10.1016/j.epsl.2005.02.025

Junttila, J., Ruikka, M., &Strand, K. (2005). Clay-mineral assemblages in high-resolution Plio-Pleistocene interval at ODP Site 1165, Prydz Bay, Antarctica. *Global and Planetary Change*, *45*(1–3), 151–163.

Klute, A. (1986). Water retention: Laboratory methods. *Methods of soil analysis: Part 1—Physical and mineralogical methods*, *1*, 635–662.

Li, F., Ginoux, P., & Ramaswamy, V. (2008). Distribution, transport, and deposition of mineral dust in the Southern Ocean and Antarctica: Contribution of major sources. *Journal of Geophysical Research*, *133*, D10207. https://doi.org/10.1029/2007JD009190

Lisiecki, L. E., & Raymo, M. E. (2005). A Pliocene-Pleistocene stack of 57 globally distributed benthic δ18O records. *Paleoceanography*, *20*, PA1003. https://doi.org/10.1029/2004PA001071

Loesdau, M., Chabrier, S., & Gabillon, A. (2014). *Hue and saturation in the RGB color space, [M]//Image and Signal Processing*. Springer International Publishing. https://doi.org/10.1007/978-3-319-07998-1_23

Lu, W., Zhao, W., Balsam, W., Lu, H., Liu, P., Lu, Z., & Ji, J. (2017). Iron mineralogy and speciation in clay-sized fractions of Chinese desert sediments. *Journal of Geophysical Research: Atmospheres*, *122*, 13,458–413,471. https://doi.org/10.1002/2017JD027733

Lyle, M. (1983). The brown-green color transition in marine sediments: A marker of the Fe (III)-Fe (II) redox boundary. *Limnology & Oceanography*, *28*(5), 1026–1033. https://doi.org/10.4319/lo.1983.28.5.1026

Martínez-Garcia, A., Rosell-Melé, A., Jaccard, S. L., Geibert, W., Sigman, D. M., & Haug, G. H. (2011). Southern Ocean dust-climate coupling over the past four million years. *Nature*, *476*(7360), 312–315. https://doi.org/10.1038/nature10310

Mathiot, P., Goosse, H., Fichefet, T., Barnier, B., & Gallée, H. (2011). Modelling the seasonal variability of the Antarctic Slope Current. *Ocean Science*, *7*(4), 455–470. https://doi.org/10.5194/os-7-455-2011

Mayer, L. M., Schick, L. L., Allison, M. A., Ruttenberg, K. C., & Bentley, S. J. (2007). Marine vs. terrigenous organic matter in Louisiana coastal sediments: The uses of bromine:organic carbon ratios. *Marine Chemistry*, *107*(2), 244–254. https://doi.org/10.1016/j.marchem.2007.07.007

Meijers, A. J. S., Klocker, A., Bindoff, N. L., Williams, G. D., & Marsland, S. J. (2010). The circulation and water masses of the Antarctic shelf and continental slope between 30 and 80°E. *Deep sea research. Part II: Topical studies in oceanography*, *57*(9-10), 723–737. https://doi.org/10.1016/j.dsr2.2009.04.019

Mix, A. C., Rugh, W., Pisias, N. G., & Veirs, S. (1992). Color reflectance spectroscopy: A tool for rapid characterization of deep-sea sediments. Proceedings of the Ocean Drilling Program, Initial Reports, Vol. 138, 67-77.

Nagao, S., & Nakashima, S. (1992). The factors controlling vertical color variations of North Atlantic Madeira Abyssal Plain sediments. *Marine Geology*, *109*(1-2), 83–94. https://doi.org/10.1016/0025-3227(92)90222-4

Nunes Vaz, R. A. N., & Lennon, G. W. (1996). Physical oceanography of the Prydz Bay region of Antarctic waters. *Deep-Sea Research Part I-Oceanographic Research Papers*, *43*(5), 603–641. https://doi.org/10.1016/0967-0637(96)00028-3

Pan, H.-J., & Chen, M.-T. (2013). Evaluating color reflectance spectral methods for estimating biogenic contents of South China Sea sediments. *Journal of Asian Earth Sciences*, *69*, 121–132. https://doi.org/10.1016/j.jseaes.2012.11.039

Pan, H.-J., Yu, P.-S., & Chen, M.-T. (2014). A marine sediment component interpretation based on diffuse reflectance spectrophotometry from northern South China Sea sediment core MD972148. *Quaternary International*, *333*, 20–25. https://doi.org/10.1016/j.quaint.2014.03.063

Passchier, S. (2011). Linkages between East Antarctic Ice Sheet extent and Southern Ocean temperatures based on a Pliocene high-resolution record of ice-rafted debris off Prydz Bay, East Antarctica. *Paleoceanography*, *26*, PA4204. https://doi.org/10.1029/2010PA002061

Passchier, S., O'Brien, P., Damuth, J., Januszczak, N., Handwerger, D., & Whitehead, J. (2003). Pliocene-Pleistocene glaciomarine sedimentation in eastern Prydz Bay and development of the Prydz trough-mouth fan, ODP Sites 1166 and 1167, East Antarctica. *Marine Geology*, *199*(3-4), 279–305. https://doi.org/10.1016/S0025-3227(03)00160-9

Pilskaln, C. H., Manganini, S. J., Trull, T. W., Armand, L., Howard, W., Asper, V. L., & Massom, R. (2004). Geochemical particle fluxes in the Southern Indian Ocean seasonal ice zone: Prydz Bay region, East Antarctica. *Deep-Sea Res. I Oceanogr. Res. Pap.*, *51*(2), 307–332. https://doi.org/10.1016/j.dsr.2003.10.010

Rein, B., & Sirocko, F. (2002). In-situ reflectance spectroscopy—Analysing techniques for high-resolution pigment logging in sediment cores. *International Journal of Earth Sciences*, *91*(5), 950–954. https://doi.org/10.1007/s00531-002-0264-0

Reitz, A., Thomson, J., Lange, G. J. D., & Hensen, C. (2006). Source and development of largemanganese enrichments above eastern Mediterranean sapropel S1. *Paleoceanography*, *21*, PA3007. https://doi.org/doi:10.1029/2005PA001169

Reynolds, R. L., Goldstein, H. L., Moskowitz, B. M., Bryant, A. C., Skiles, S. M., Kokaly, R. F., et al. (2014). Composition of dust deposited to snow cover in the Wasatch Range (Utah, USA): Controls on radiative properties of snow cover and comparison to some dust-source sediments. *Aeolian Research*, *15*, 73–90. https://doi.org/10.1016/j.aeolia.2013.08.001

Röthlisberger, R., Crosta, X., Abram, N. J., Armand, L., & Wolff, E. W. (2010). Potential and limitations of marine and ice core sea ice proxies: An example from the Indian Ocean sector. *Quaternary Science Reviews*, *29*(1-2), 296–302. https://doi.org/10.1016/j.quascirev.2009.10.005

Weber, M. E., Kuhn, G., Sprenk, D., Rolf, C., Ohlwein, C., & Ricken, W. (2012). Dust transport from Patagonia to Antarctica—A new stratigraphic approach from the Scotia Sea and its implications for the last glacial cycle. *Quaternary Science Reviews*, *36*, 177–188. https://doi.org/10.1016/j.quascirev.2012.01.016

Weber, M. E., Tougiannidis, N., Kleineder, M., Bertram, N., Ricken, W., Rolf, C., et al. (2010). Lacustrine sediments document millennial-scale climate variability in northern Greece prior to the onset of the Northern Hemisphere glaciation. *Palaeogeography, Palaeoclimatology, Palaeoecology*, *291*(3-4), 360–370. https://doi.org/10.1016/j.palaeo.2010.03.007

Wei, J. H., Finkelstein, D. B., Brigham-Grette, J., Castaneda, I. S., & Nowaczyk, N. (2014). Sediment color reflectance spectroscopy as a proxy for wet/dry cycles at Lake El'gygytgyn, Far East Russia, during Marine Isotope Stages 8 to 12. *Sedimentology*, *61*(6), 1793–1811. https://doi.org/10.1111/sed.12116

Williams, G., Bindoff, N., Marsland, S., & Rintoul, S. (2008). Formation and export of dense shelf water from the Adlie Depression, East Antarctica. *Journal of Geophysical Research*, *113*(C04039). https://doi.org/10.1029/2007JC004346

Wu, J., Liu, Z., & Zhou, C. (2013). Provenance and supply of Fe-enriched terrigenous sediments in the western equatorial Pacific and their relation to precipitation variations during the Late Quaternary. *Global and Planetary Change*, *108*, 56–71. https://doi.org/10.1016/j.gloplacha.2013.06.002

Wu, L. (2017). Late Quaternary climate variability recorded in sediments off Prydz Bay East Antarctica (PHD thesis) (pp. 91–100). China: Tongji University.

Wu, L., Wang, R., Xiao, W., Ge, S., Chen, Z., & Krijgsman, W. (2017). Productivity-climate coupling recorded in Pleistocene sediments off Prydz Bay (East Antarctica). *Palaeogeography, Palaeoclimatology, Palaeoecology*, *485*, 260–270. https://doi.org/10.1016/j.palaeo.2017.06.018

Wu, L., Wang, R., Xiao, W., Krijgsman, W., Li, Q., Ge, S., & Ma, T. (2018). Late Quaternary deep stratification-climate coupling in the Southern Ocean: Implications for changes in abyssal carbon storage. *Geochemistry, Geophysics, Geosystems*, *19*, 379–395. https://doi.org/10.1002/2017GC007250

Yabuki, T., Suga, T., Hanawa, K., Matsuoka, K., Kiwada, H., & Watanabe, T. (2006). Possible source of the Antarctic bottom water in the Prydz Bay region. *Journal of Oceanography*, *62*(5), 649–655. https://doi.org/10.1007/s10872-006-0083-1

Yang, S., Tang, M., Yim, W. W. S., Zong, Y., Huang, G., Switzer, A. D., & Saito, Y. (2011). Burial of organic carbon in Holocene sediments of the Zhujiang (Pearl River) and Changjiang (Yangtze River) estuaries. *Marine Chemistry*, *123*(1-4), 1–10. https://doi.org/10.1016/j.marchem.2010.07.001

Yang, S. L., & Ding, Z. L. (2003). Color reflectance of Chinese loess and its implications for climate gradient changes during the last two glacial-interglacial cycles. *Geophysical Research Letters*, *30*(20), 2058. https://doi.org/10.1029/2003GL018346

Ziegler, M., Jilbert, T., De Lange, G. J., Lourens, L. J., & Reichart, G. J. (2013). Bromine counts from XRF scanning as anestimate of the marine organic carbon content of sediment cores. *Geochemistry Geophysics Geosystems*, *9*(5). https://doi.org/10.1029/2007GC001932